Electronic Supplemental Information for

Stabilizing Three-Center Single-Electron Metal-Metal Bond in a Fullerene Cage

Fei Jin,[a,#] Jinpeng Xin,[a,#] Runnan Guan,[a] Xiao-Ming Xie,[b] Muqing Chen,[a,*] Qianyan Zhang,[b,*] Alexey A. Popov,[c,*] Su-Yuan Xie,[b] and Shangfeng Yang[a,*]

Table of Contents

S1. Experimental Section ***.....S2***
S2. Isolation of $Dy_3C_2@I_h(7)$-C_{80} ***.....S3***
S3. Estimation of the relative yield of $Dy_3C_2@I_h(7)$-C_{80}. ***.....S4***
S4. X-ray single crystal data of $Dy_3C_2@I_h(7)$-C_{80}. ***.....S5***
S5. Computational analysis of molecular srtucture and bonding in $Dy_3C_2@I_h(7)$-C_{80}. ***.....S7***
S6. Calculated MO levels and charged states of $Dy_3C_2@C_{80}$ and $Sc_3C_2@C_{80}$. ***.....S18***
S7. UV-vis-NIR spectroscopic data and cyclic voltammograms of $Dy_3C_2@I_h(7)$-C_{80} in different scanning regions. ***.....S19***
References ***.....S21***

S1. Experimental Section

Materials

All materials including dry solvents were obtained from commercial suppliers and used without further purification. Dy_2O_3 (99.99%) was purchased from Suzhou Rare Earth New Materials Co., Ltd, TiO_2 (99.99%) were obtained from Sinopharm Chemical Reagent Co., Ltd, Graphite rods (SP) were purchased from Sinosteel Shanghai New Graphite Material Co., Ltd.

Synthesis, isolation and spectroscopic characterizations of $Dy_3C_2@I_h(7)$-C_{80}. $Dy_3C_2@I_h(7)$-C_{80} were synthesized in a modified Krätschmer-Huffman fullerene generator by vaporizing composite graphite rods (Φ 8 × 100 mm) containing a mixture of Dy_2O_3, TiO_2 and graphite powder (molar ratio of Dy : Ti : C = 1 : 1 : 15) with the addition of 10 mbar N_2 into 200 mbar He. The as-produced soot was Soxhlet-extracted by CS_2 for 24 h, and the resulting brown-yellow solution was distilled to remove CS_2 and then immediately re-dissolved in toluene and subsequently passed through a 0.2 μm Telflon filter (Sartorius AG, Germany) for HPLC separation.

The isolation of $Dy_3C_2@I_h(7)$-C_{80} was successfully isolated from fraction A which was isolated running in a 20 x 250 mm 5PYE column (Figure S1a) from $Dy_2O_3/TiO_2/N_2$ extracts (mixed with a small number of $Dy_2O_3/TiO_2/Fe_3N$ extracts) (flow rate 15.0 ml/min; inject volume 15 ml; toluene as eluent; 40 ^oC) by the following two-step HPLC. In the first-step HPLC isolation running in a 20 × 250 mm Buckyprep-M column and the chromatogram is shown in Figure S1b (flow rate 15.0 ml/min; inject volume 15 ml; toluene as eluent; 40 ℃), Fraction **A-3** was collected and then subjected to the second-step HPLC running in a 10 × 250 mm 5PBB column and the chromatogram is shown in Figure S1c (flow rate 5.0 ml/min; inject volume 5 ml; toluene as eluent; 25 ℃). Pure $Dy_3C_2@I_h(7)$-C_{80} (fraction **A-3-3**) was obtained, for which the purities of the isolated $Dy_3C_2@I_h(7)$-C_{80} were further checked by laser desorption/ionization time-of-flight (LD-TOF) mass spectroscopic (MS) analysis (Biflex III, Bruker Daltonics Inc., Germany) shown in Figure 1a.

UV-vis-NIR spectra were recorded on a UV-vis-NIR 3600 spectrometer (Shimadzu, Japan) using a quartz cell of 1 mm layer thickness and 1 nm resolution with the samples dissolved in toluene.

Electrochemical Study. Electrochemical study was performed in *o*-dichlorobenzene (*o*-DCB, anhydrous, 99%, Aldrich). The supporting electrolyte was tetrabutylammonium hexafluorophosphate ($TBAPF_6$, puriss. electrochemical grade, Fluka), which was dried under reduced pressure at 340 K for 24 h and stored in glovebox prior to use. Cyclic voltammogram experiments were performed with a CHI 660 potentiostat (CH Instrument, USA) at room temperature in a glovebox. A standard three-electrode arrangement of a platinum (Pt) wire as working electrode, a platinum coil as counter electrode, and a silver wire as a pseudoreference electrode was used. In a comparison experiment, ferrocene (Fc) was added as the internal standard and all potentials are referred to the Fc/Fc^+ couple.

X-ray crystallographic studies. Crystal growth was accomplished by a mixing solution of clusterfullerenes and DPC. After the two solutions diffused together over a period of one-two weeks, small black crystals suitable for X-ray crystallographic study formed upon a slow evaporation of solvent. The crystallographical characterization was performed at 100 K in beamline station BL17B at Shanghai Synchrotron Radiation Facility. The structure was refined using all data (based on F^2) by SHELX 2014[20] within Olex2. And a part of the solvent disorder was dealed with using Program SQUEEZE if needed.[21] Crystallographic data of $Dy_3C_2@I_h(7)$-C_{80}·2(DPC)·3(C_7H_8) can be obtained free of charge from the Cambridge Crystallographic Data Center (CCDC number: 2057452).

S2. Isolation of $Dy_3C_2@I_h(7)$-C_{80}

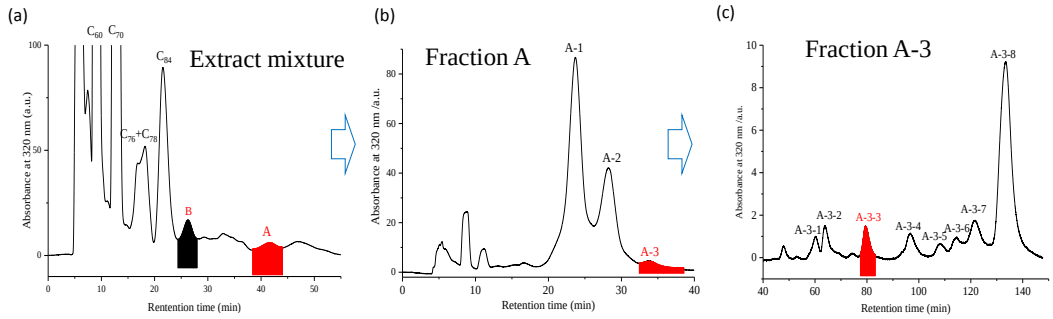

Figure S1. Isolation scheme of $Dy_3C_2@I_h(7)$-C_{80}. (a) HPLC profile of the $Dy_2O_3/TiO_2/N_2$ fullerene extract mixture (20×250 mm 5PYE column; flow rate: 15 mL·min^{-1}; injection volume: 15 mL; toluene as eluent; 40 °C). Fraction **A** was collected and then subjected to the next-step HPLC isolation. Fraction **B** contains C_{86}, $DyCN@C_{2n}$ (2n=76, 82) and $Dy_3N@C_{80}$. (b) HPLC profile of fraction **A** (20 × 250 mm Buckyprep-M column, flow rate: 15 mL·min^{-1}; injection volume: 15 mL; toluene as eluent; 40 °C), Subfractions **A-1**, **A-2** correspond to C_{94}, Dy_2C_{90}+DyC_{92}, respectively. (c) HPLC profile of fraction **A-3** (10 × 250 mm 5PBB column, flow rate: 5 mL·min^{-1}; injection volume: 5 mL; toluene as eluent; 25 °C). Subfractions **A-3-1, A-3-2, A-3-4, A-3-5, A-3-6, A-3-7, A-3-8** correspond to DyC_{84}, Dy_2C_{82}, DyC_{90}, Dy_2C_{90}, DyC_{92}(I), DyC_{92}(II), DyC_{94}+$Dy_3N@C_{88}$.

S3. Estimation of the relative yield of $Dy_3C_2@I_h(7)$-C_{80}.

Table S1. Assignment of each (sub)fraction and their relative abundance.

Fraction	Sub-fraction	Major component	Relative abundance
B	B-1	C_{86}	63.38 %
	B-2	$DyCN@C_{76/82}$	17.51 %
	B-3	**$Dy_3N@C_{80}$**	**19.11 %**
A	A-1	C_{94}	64.12 %
	A-2	Dy_2C_{90}+DyC_{92}	33.65 %
	A-3	**$DyC_{92/94}$+$Dy_3N@C_{88}$**	**2.23 %**
A-3	A-3-1	DyC_{84}	3.73 %
	A-3-2	Dy_2C_{82}	6.88 %
	A-3-3	**$Dy_3C_2@C_{80}$**	**6.69 %**
	A-3-4	DyC_{90}	7.52 %
	A-3-5	Dy_2C_{90}	3.55 %
	A-3-6	DyC_{92}(I)	4.82 %
	A-3-7	DyC_{92}(II)	11.39 %
	A-3-8	DyC_{94}+$Dy_3N@C_{88}$	55.23 %

Given that relative yield of fraction **A:B is ~2:5**, the relative yield of $Dy_3C_2@I_h(7)$-C_{80} to $Dy_3N@C_{80}$ can be calculated as:

$$Dy_3C_2@I_h(7)\text{-}C_{80}:Dy_3N@C_{80} = (6.69\times 2.23\%) : (19.11\% \times 2.5) \approx 1 : 320.2$$

S4. X-ray single crystal data of $Dy_3C_2@I_h(7)$-C_{80}.

Table S2. Crystal and structure data of $Dy_3C_2@I_h(7)$-C_{80} at 100 K.

Crystal	$Dy_3C_2@I_h(7)$-C_{80}
Formula weight	3550.76
Wavelength(λ, Å)	0.71073
Temperature/K	100(2)
Crystal system	monoclinic
Space group	$P2_1/c$
a, Å	14.761
b, Å	32.102
c, Å	32.240
α, deg	90
β, deg	101.88
γ, deg	90
Volume, $Å^3$	14949.9
Z	4
Unique data(R_{int})	25480(0.069)
Parameters	2371
Restraints	1083
Observed data($I>2\sigma(I)$)	20088
$R1^a$ (observed)	0.0907
$wR2^b$ (all data)	0.2709

[a] For data with $I>2\sigma(I)$, $RI=1||F_o|-|F_c||/\Sigma|F_o|$.
[b] For all data, wR2=$\{\Sigma[w(F_o^2-F_c^2)^2])/\Sigma[w(F_o^2)^2]\}^{1/2}$.

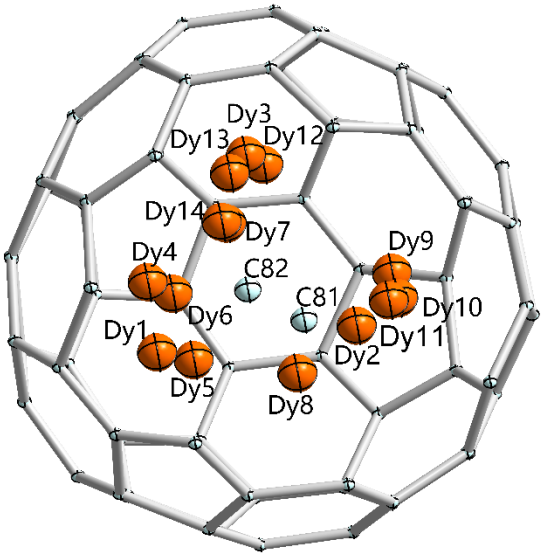

Figure S2. All disordered dysprosium sites in $Dy_3C_2@I_h$-C_{80} relative to cage orientation. The fractional occupancies are 0.482(2), 0.501(2), 0.429(3), 0.175(2), 0.205(2), 0.138(2), 0.1174(19), 0.073(2), 0.238(3), 0.138(3), 0.051(2), 0.139(3), 0.188(3), 0.126(2) for Dy1, Dy2, Dy3, Dy4, Dy5, Dy6, Dy7, Dy8, Dy9, Dy10, Dy11, Dy12, Dy13, and Dy14, respectively.

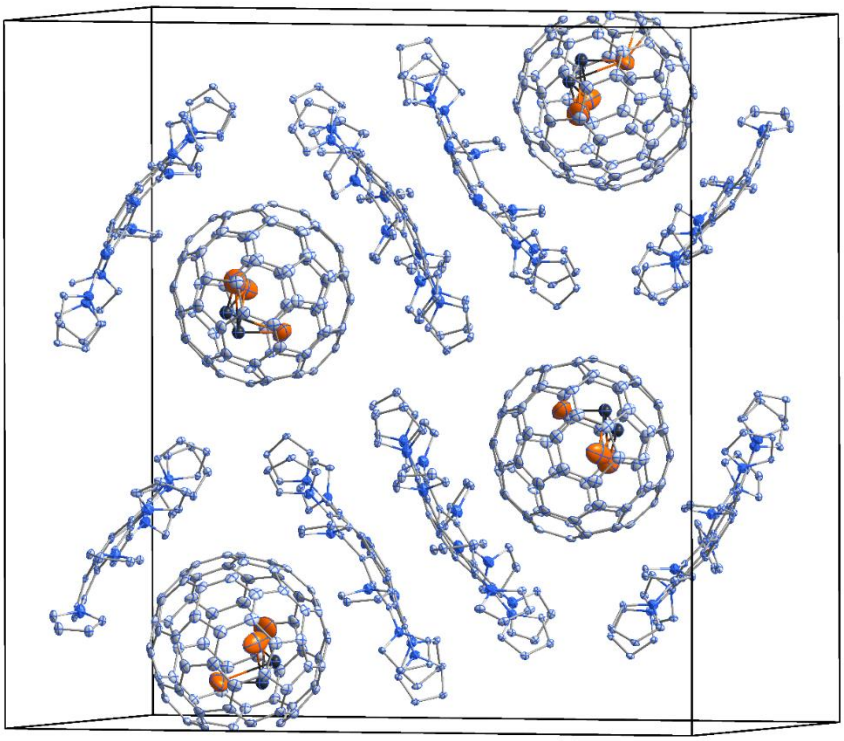

Figure S3. The molecular packing of $Dy_3C_2@I_h(7)$-C_{80}·2DPC. Only the major Dy_3C_2 site is shown. Solvent molecules and H atoms are omitted for clarity.

S5. Computational analysis of molecular structure and bonding in $Dy_3C_2@I_h(7)$-C_{80}.

1) DFT calculations of molecular structures:

A reliable description of molecules with partially-filled 4f-shell requires expensive multiconfigurational approaches and is hardly possible for a molecule like $Dy_3C_2@C_{80}$ at this moment. Single-determinant DFT calculations with explicit consideration of 4f electrons are not very reliable, and to avoid this problem we therefore preferred to use 4f-in-core effective core potential with ECP55MWB-II basis set to treat Dy atoms.[S1, S2] For Sc and carbon atoms, def2-TZVPP basis was used.[S3] Number of basis functions and contraction schemes are listed below in {s/p/d/f/g} form. Calculations were performed with Orca package[S4] using PBE functional.[S5]

C: {62111/411/11/1}
Sc: {842111/63111/4111/11/1}
Dy: {311111/31111/21111/111/11}

In addition to limited Dy calculations used for property evaluation, we also performed a broader search of rotational conformers for $Y_3C_2@C_{80}$ using Priroda code[S6, S7] with implemented basis set of TZ2P quality for carbon and SBKJC-type effective core potential for Y. Calculations showed several conformers different in the relative orientation of the Y_3C_2 cluster within the fullerene cage. The structure of the cluster remains almost intact, relative energies of such rotational conformers are close within few kJ/mol. Priroda code was also used to locate the transition state between bat ray and trifoliate configurations.

Table S3. Relative energies (kJ mol^{-1}) of different cluster configurations in $Y_3C_2@C_{80}$ and $Dy_3C_2@C_{80}$

	bat ray	trifoliate	transition state
$Y_3C_2@C_{80}$	0.0	60.2	105.6
$Dy_3C_2@C_{80}//Y_3C_2@C_{80}$[a]	0.0	89.4	139.8[b]
$Dy_3C_2@C_{80}$	0.0	89.9	

[a] Single-point energy calculation for $Dy_3C_2@C_{80}$ in geometry optimized for $Y_3C_2@C_{80}$
[b] Figure 3 uses this value for the relative energy of TS configuration

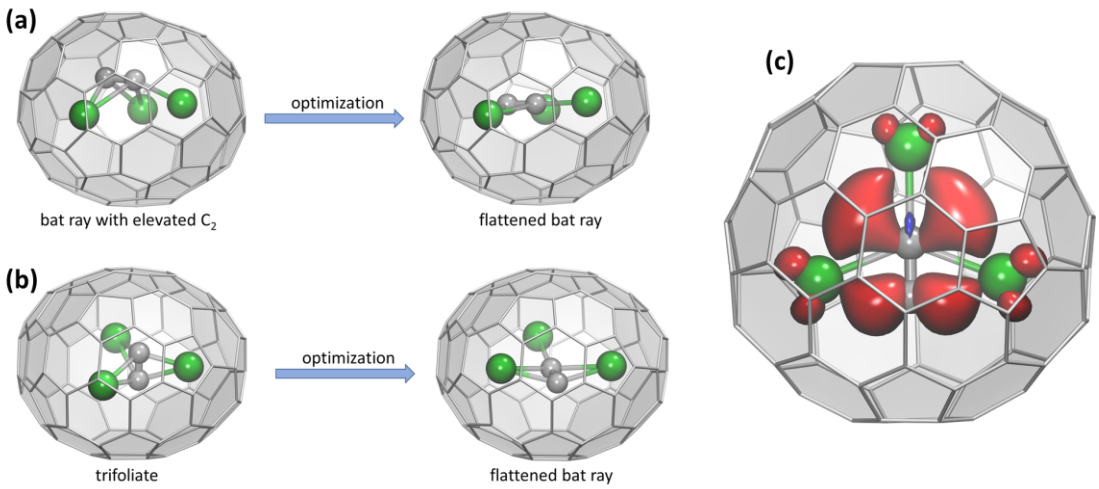

Figure S4. (a,b) DFT optimization of $Y_3C_2@C_{88}$ with different starting configurations of the Y3C2 cluster, leading to flattened bat ray configuration after optimization. (c) Spin-density distribution in DFT-optimized $Dy_3C_2@C_{88}$ with flattened bat ray configuration of Dy_3C_2 cluster.

2) Canonical molecular orbitals:

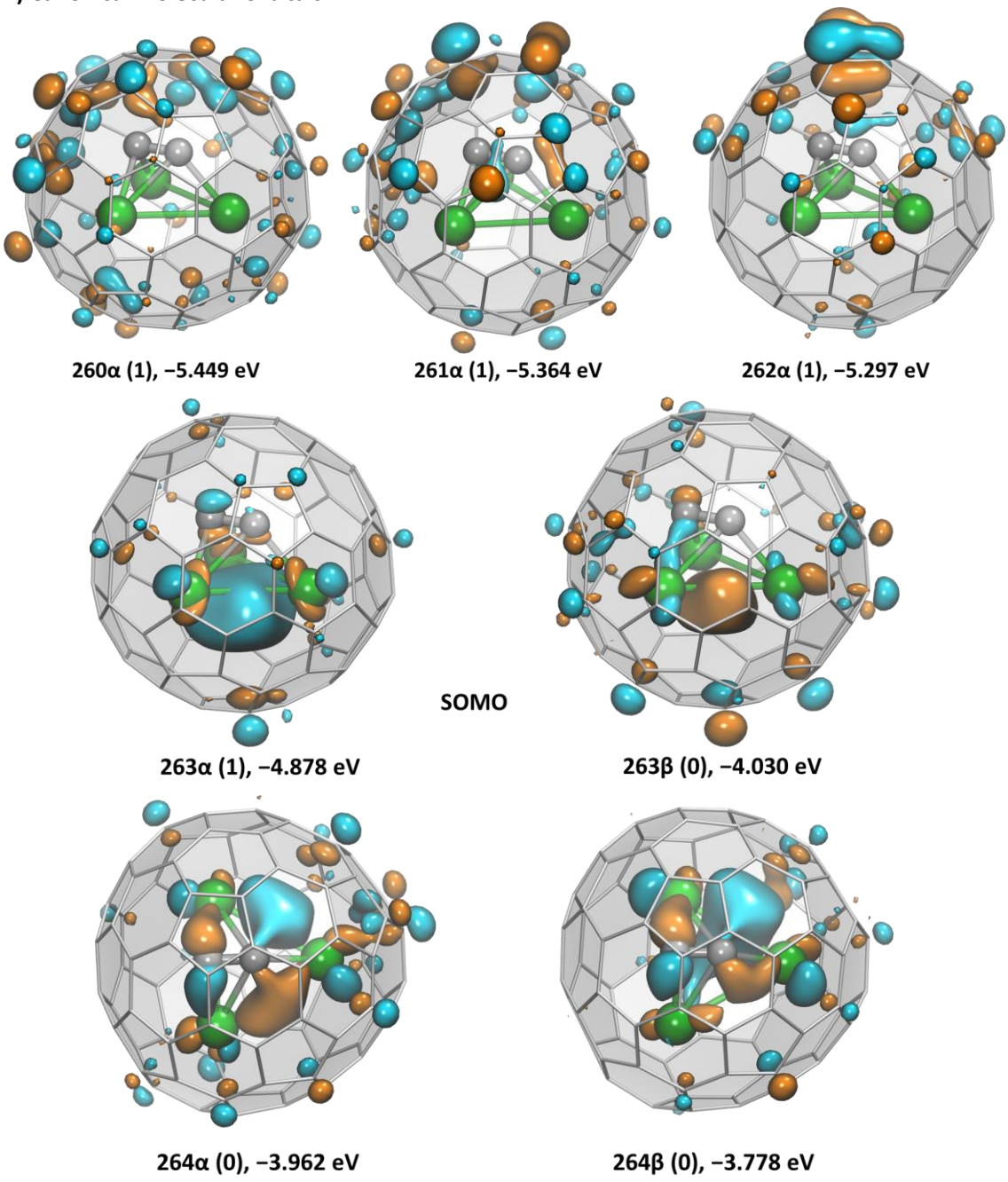

Figure S5. Canonical Kohn-Sham molecular orbitals of $Dy_3C_2@C_{80}$ in selected energy range. Occupation of a given orbital (1 for occupied and 0 for unoccupied) is given in parentheses followed by the orbital energy in eV. For SOMO and some low-energy unoccupied orbitals, α and β orbital are shown as they have somewhat different energies and shapes because of the spin polarization. For other orbitals, β orbitals are not shown as they are similar to α counterparts.

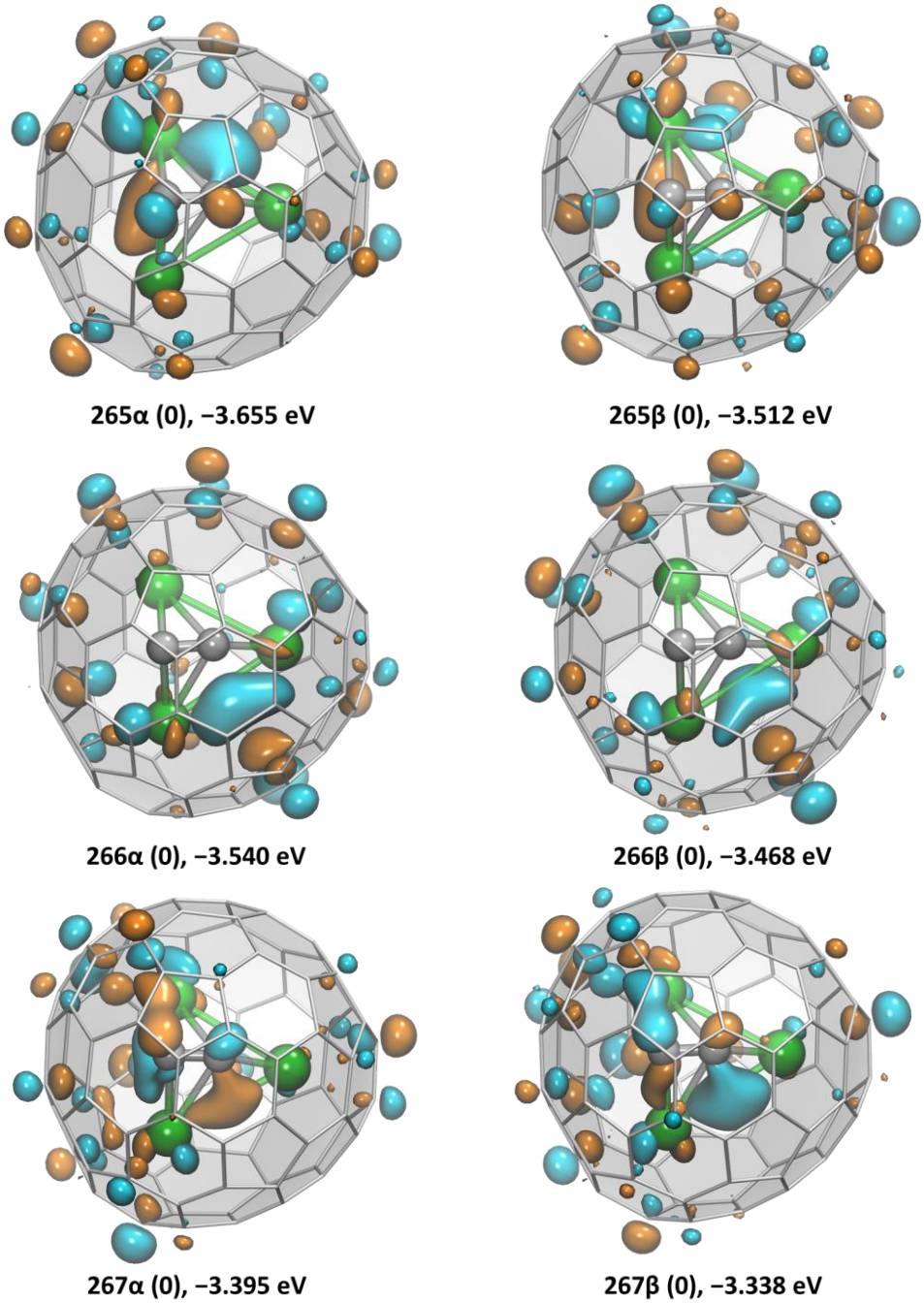

Figure S5. (continued) Canonical Kohn-Sham molecular orbitals of $Dy_3C_2@C_{80}$ in selected energy range. Occupation of a given orbital (1 for occupied and 0 for unoccupied) is given in parentheses followed by the orbital energy in eV. For SOMO and some low-energy unoccupied orbitals, α and β orbital are shown as they have somewhat different energies and shapes because of the spin polarization. For other orbitals, β orbitals are not shown as they are similar to α counterparts.

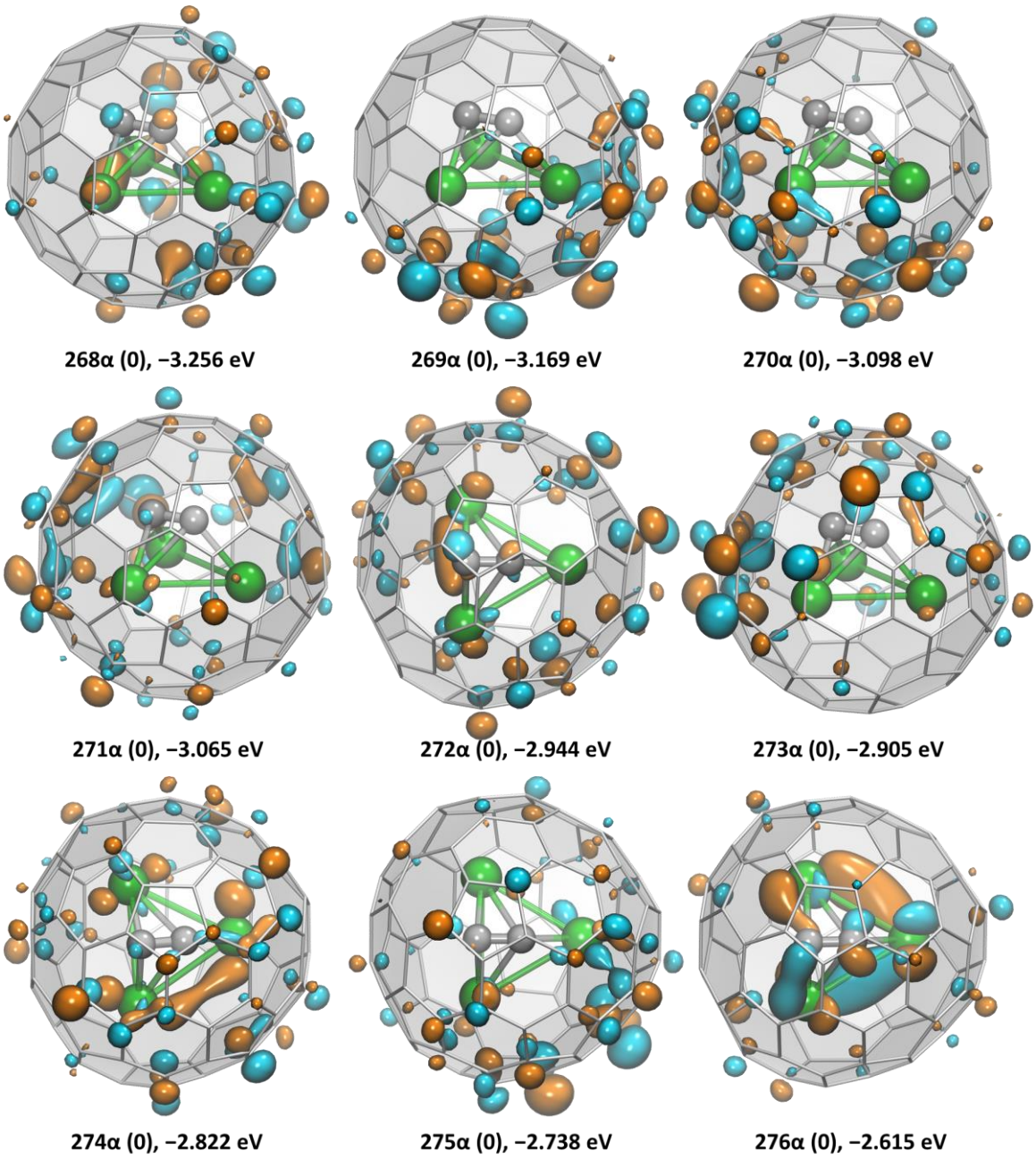

Figure S5. (continued) Canonical Kohn-Sham molecular orbitals of $Dy_3C_2@C_{80}$ in selected energy range. Occupation of a given orbital (1 for occupied and 0 for unoccupied) is given in parentheses followed by the orbital energy in eV. For SOMO and some low-energy unoccupied orbitals, α and β orbital are shown as they have somewhat different energies and shapes because of the spin polarization. For other orbitals, β orbitals are not shown as they are similar to α counterparts.

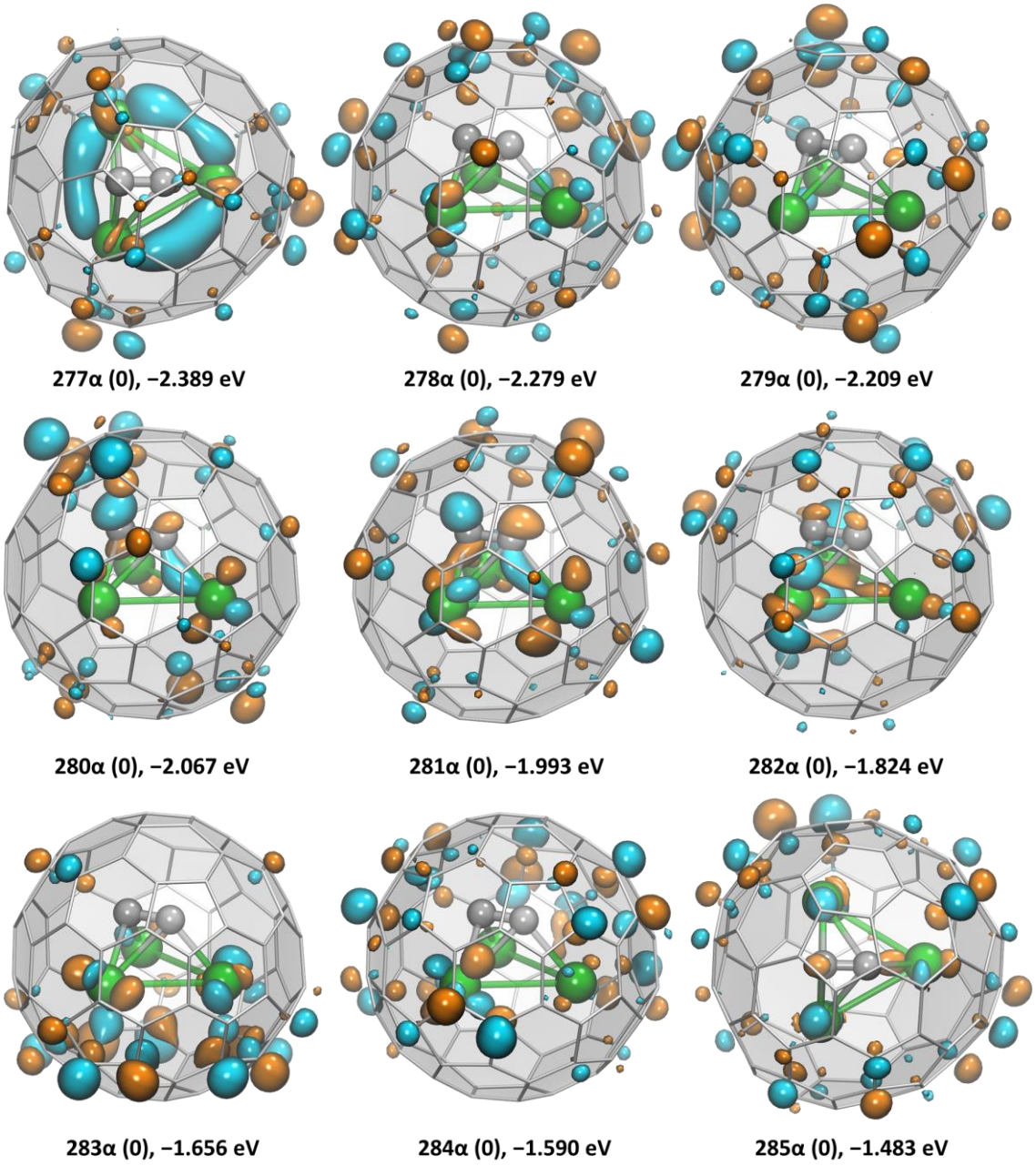

Figure S5. (continued) Canonical Kohn-Sham molecular orbitals of $Dy_3C_2@C_{80}$ in selected energy range. Occupation of a given orbital (1 for occupied and 0 for unoccupied) is given in parentheses followed by the orbital energy in eV. For SOMO and some low-energy unoccupied orbitals, α and β orbital are shown as they have somewhat different energies and shapes because of the spin polarization. For other orbitals, β orbitals are not shown as they are similar to α counterparts.

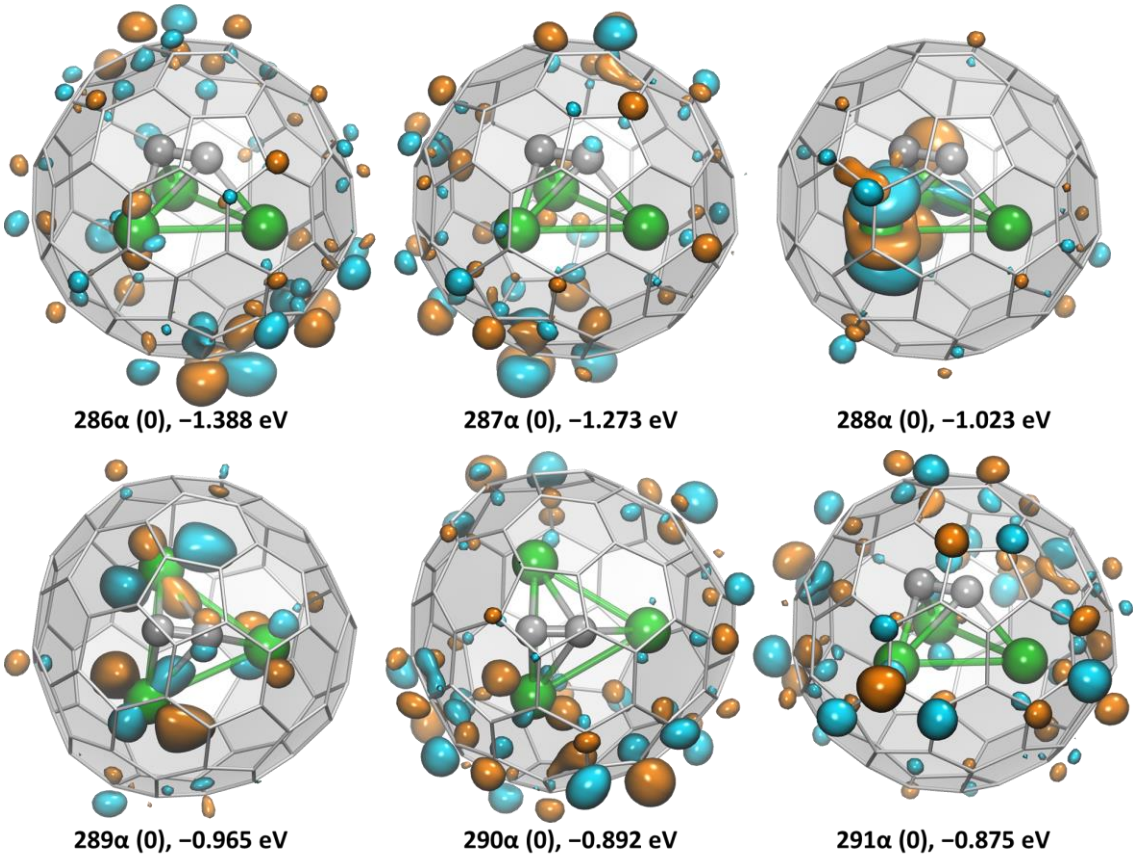

Figure S5. (continued) Canonical Kohn-Sham molecular orbitals of $Dy_3C_2@C_{80}$ in selected energy range. Occupation of a given orbital (1 for occupied and 0 for unoccupied) is given in parentheses followed by the orbital energy in eV. For SOMO and some low-energy unoccupied orbitals, α and β orbital are shown as they have somewhat different energies and shapes because of the spin polarization. For other orbitals, β orbitals are not shown as they are similar to α counterparts.

3) Localized molecular orbitals:

For a more illustrative analysis of the bonding, we performed localization of molecular orbitals with Pipek-Mezey approach.[S8] Localized orbitals give more condensed representation of the orbital than (delocalized) canonical orbitals. Figures S4 and S5 show PM-localized orbitals for the two configurations of Dy_3C_2 cluster in $Dy_3C_2@C_{80}$.

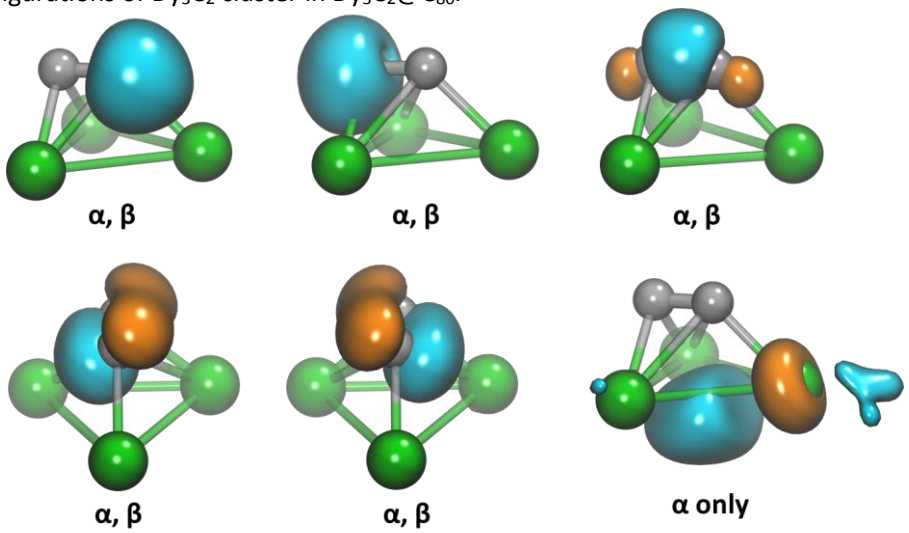

Figure S6. PM-localized orbitals of the bat ray configuration of Dy_3C_2 cluster in $Dy_3C_2@C_{80}$. One σ-bonding and two π-bonding orbitals of C_2 unit are two-fold occupied (both α and β components are present). The only singly-occupied cluster-based orbital (only α component is present) is the 3-center Dy–Dy–Dy bonding MO (it has similar shape to the canonical MO).

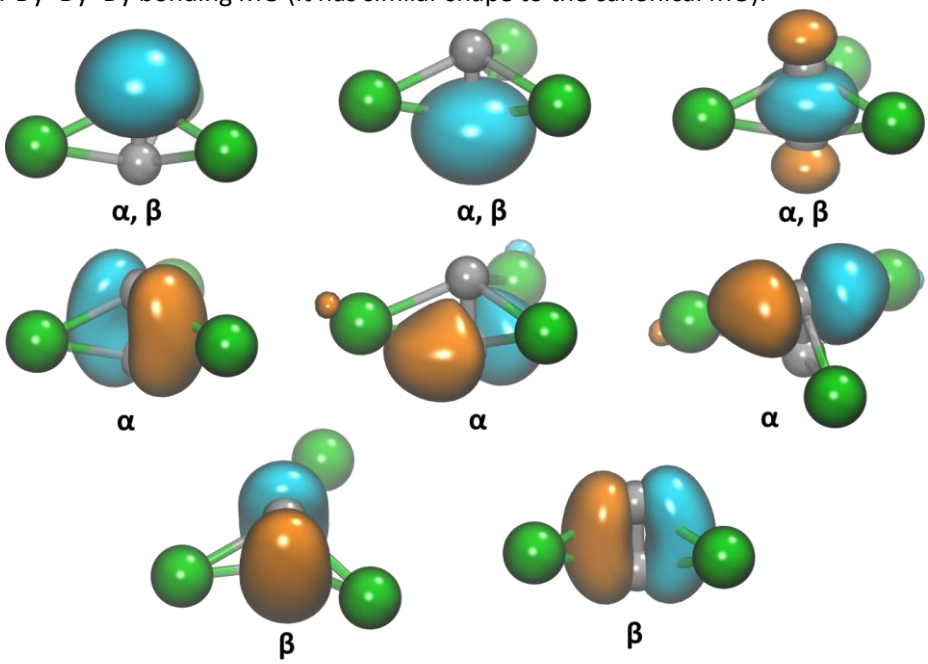

Figure S7. PM-localized orbitals of the trifoliate configuration of Dy_3C_2 cluster in $Dy_3C_2@C_{80}$. The σ-bonding orbitals of C_2 unit is two-fold occupied (both α and β components are present). π-bonding orbitals of C_2 unit are more complex. One can see two β orbitals and one α orbital with clear π-bonding character. There are two other α orbitals with mixed C_2-π-bonding/5d-π bonding character.

4) Spin density distribution:

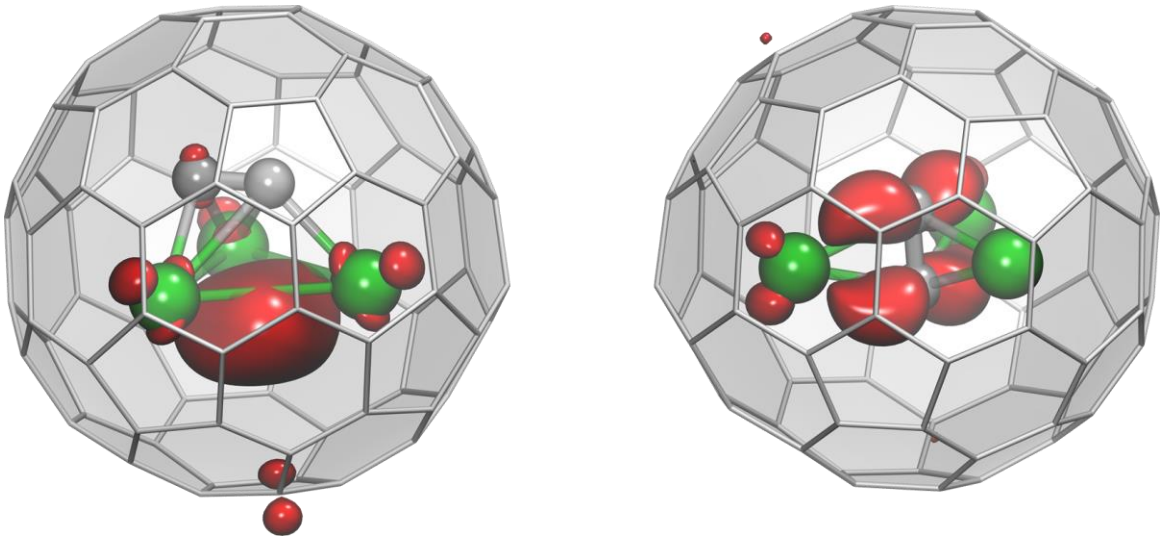

Figure S8. DFT-computed spin density distribution in $Dy_3C_2@C_{80}$ with bat ray (left) and trifoliate (right) cluster configurations. Note that the use of 4f-in-core potential limits the spin density to the valence part only, whereas 4f-shell is not represented.

5) QTAIM analysis of charge distribution and bonding:

Topological analysis of the electron density was performed using Bader Quantum Theory of Atoms in Molecules (QTAIM).[S9] QTAIM of the electron density required full-electron calculations, whereas the use of ECP basis may lead to artefacts. Among rare-earth metals of comparable ionic radius, Y and Gd analogs can be described by a single-determinant wavefunction and can be therefore reliably treated with full-electron DFT calculations. We thus performed QTAIM analysis of $Y_3C_2@C_{80}$ and $Gd_3C_2@C_{80}$ using DFT-optimized $Dy_3C_2@C_{80}$ geometry. Electron density was computed at the PBE level with DKH scalar-relativistic correction as implemented in Orca with def2-SVP basis set for carbon, and SARC-DKH-TZVP basis sets for Gd and Y.[S4, 10] QTAIM calculations were performed with the AIMAll package.[S11]

From the large set of parameters provided by QTAIM, we focus here on atomic charges and delocalization indices (the number of electron pairs shared between two atoms aka QTAIM bond orders). Figure S7 compares bat ray and trifoliate cluster configurations for $Y_3C_2@C_{80}$ and $Gd_3C_2@C_{80}$ along with the atomic charges and delocalization indices. For Y analog, calculations predict more ionic nature (more positive/negative atomic charges of metals/carbon, and smaller metal-carbon bond orders), but the overall bonding situation in $Y_3C_2@C_{80}$ and $Gd_3C_2@C_{80}$ is similar. The bat ray configuration has less positive/negative atomic charges of metals/carbons than in the trifoliate configuration. It points to the higher covalency in the bat ray configuration. The C–C bond order in the bay ray structure (2.35 for Y and 2.31 for Gd) is higher than in the trifoliate one (2.03 for Y and 1.95 for Gd), agreeing with a smaller formal negative charge (C_2^{2-} versus C_2^{3-}).

In the trifoliate configuration, each metal is bonded to the C_2 group in η^2-manner. Note however that two of three metals have somewhat higher M–C bond orders, which also corresponds to the shape of localized MOs, which have large contributions from two metals (Fig. S5). Metal-metal interactions in the trifoliate configuration are negligible (delocalization indices 0.03–0.04 for Y and 0.04–0.05 for Gd). In the bat ray configuration, two metals also have η^2-bonding (M–C bond orders near 0.35–0.41/0.21–0.24), whereas one shows η^1-bonding to only one carbon (M–C bond order 0.47 for Y and 0.52 for Gd). Most importantly, QTAIM analysis reveals considerable M–M delocalization indices in the bat ray configuration. M–M bond orders of 0.12/0.14/0.16 for Y and 0.14/0.15/0.17 for Gd sum up to 0.41 (Y) or 0.45 (Gd) electron pairs shared between three metal atoms, perfectly corresponding to the three center-one electron bond.

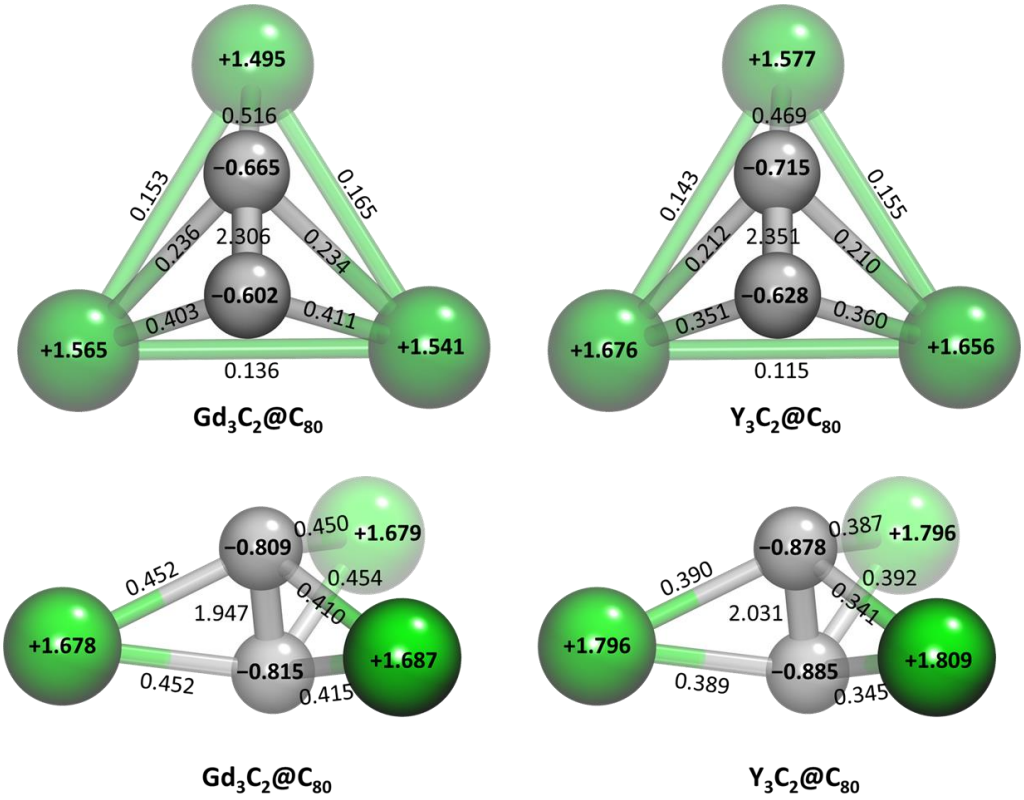

Figure S9. QTAIM atomic charges and delocalization indices (bond orders) in $Gd_3C_2@C_{80}$ and $Y_3C_2@C_{80}$ with bat ray (upper row) and trifoliate (bottom row) cluster configurations (atomic coordinates are optimized for $Dy_3C_2@C_{80}$).

S6. MO levels and charged states of $Dy_3C_2@C_{80}$ and $Sc_3C_2@C_{80}$

Frontier MO energies of $Dy_3C_2@C_{80}$ and $Sc_3C_2@C_{80}$ are compared in Table S5. Note that both HOMO and LUMO here correspond to the occupied and unoccupied components of the SOMO (see Fig. 3 in the main text for MO levels of other orbitals). The HOMO-LUMO gap of $Dy_3C_2@C_{80}$ is higher than in $Sc_3C_2@C_{80}$, which may be also reflected in their electrochemical properties, i.e. the electrochemical gap of $Dy_3C_2@C_{80}$ is higher than in $Sc_3C_2@C_{80}$. However, considering only MO energies, one might expect that the oxidation potential of $Sc_3C_2@C_{80}$ should be more positive than in $Dy_3C_2@C_{80}$, which does not agree with the experimental observation. However, experimental redox processes in fact correspond not to the arbitrary orbital energies but to the energy differences between the charged state. Thus, we performed DFT optimization of $Dy_3C_2@C_{80}$ and $Sc_3C_2@C_{80}$ in their cation and anionic states, and then also performed single-point energy calculations in o-DCB modeled as polarized continuum (C-PCM model). Table S5 also compares electron affinities (*EA*) and ionization potential (*IP*) of the two molecules in gas phase and their values with solvation correction (which correspond to redox potentials). Calculations in the gas phase show that although HOMO level of $Sc_3C_2@C_{80}$ is lower in energy than in $Dy_3C_2@C_{80}$, *IP* of $Sc_3C_2@C_{80}$ is smaller than that of $Dy_3C_2@C_{80}$. In agreement with earlier results,[S12] we also found that the Sc_3C_2 cluster in $Sc_3C_2@C_{80}^+$ attains the trifoliate configuration. With solvation correction, computed electrochemical gap of $Dy_3C_2@C_{80}$ is 1.10 V (versus experimental 1.18 V) and 0.61 V in $Sc_3C_2@C_{80}$ (versus experimental 0.47 V).

Table S4. DFT-computed MO energies, ionization potential (IP), and electron affinities (EA) of $Dy_3C_2@C_{80}$ and $Sc_3C_2@C_{80}$ in gas phase and in o-DCB (eV).

	$Dy_3C_2@C_{80}$	**$Sc_3C_2@C_{80}$**
E_{ox}(exp), V[a]	+0.19	−0.03
E_{red}(exp), V[a]	−0.99	−0.50
ΔE_{EC}(exp), V	1.18	0.47
SOMO(occ)	−4.878	−4.998
SOMO(unocc)	−4.030	−4.500
ΔE_{MO}	0.848	0.498
EA(gas)	2.786	3.221
IP(gas)	6.129	5.954
Δ(*IP*–*EA*)	3.343	2.733
ΔE_{solv}(0)	−0.066	−0.097
ΔE_{solv}(−1)	−1.047	−1.047
ΔE_{solv}(+1)	−1.329	−1.277
EA(oDCB) ≡ E_{red}[b]	3.768	4.162
IP(oDCB) ≡ E_{ox}[v]	4.865	4.774
ΔE_{EC}(oDCB)	1.098	0.612

[a] redox potentials in *o*-DCB versus $Fe(Cp)_2^{+/0}$ pair;
[b] absolute potentials

Table S5. DFT-optimized bond lengths (Å) in bat ray configuration of $Dy_3C_2@C_{80}$ in cation, neutral, and anionic states.

	q = +1	q = 0	q = −1
Dy1–Dy2	3.542	3.408	3.320
Dy1–Dy3	3.668	3.441	3.363
Dy2–Dy3	3.472	3.382	3.366
Dy1–C81	2.545	2.686	2.692
Dy1–C82	2.372	2.357	2.361
Dy2–C81	2.314	2.325	2.334
Dy3–C81	2.608	2.677	2.666
Dy3–C82	2.350	2.365	2.370
C81–C82	1.260	1.256	1.256

Comparison of the bond lengths in Dy_3C_2 cluster in different charge state of the molecule (Table S6) shows that Dy–Dy distances are most affected. In the anion, the distances become shorter whereas in the cation they are longer than in the neutral state. Changes of Dy–C and C–C bond are less pronounced. These changes agree well with the population and depopulation of the Dy–Dy–Dy bonding orbital.

S7. UV-vis-NIR spectroscopic data and cyclic voltammograms of $Dy_3C_2@I_h(7)$-C_{80} in different scanning regions.

Table S6. Redox Potentials (V vs. Fc/Fc^+), electrochemical gaps (ΔE_{EC}) of $Dy_3C_2@I_h$-C_{80} and other reported $M_3C_2@I_h(7)$-C_{80} (M=Sc, Ti).

sample	$E_{1/2}$ (V vs Fc/Fc^+)				ΔE_{EC} / V [a]	Absorption onset (λ_{onset},nm)	$\Delta E_{optical}$/ eV [b]	Ref.
	Reduction steps (E_{red})			Oxidation step (E_{ox})				
	first	second	third	first				
$Dy_3C_2@I_h(7)$-C_{80}	-0.99	-1.65 [c]	/	+0.19	1.18	835	1.49	This work
$Sc_3C_2@I_h(7)$-C_{80}	-0.50	-1.64	/	-0.03	0.47	900[d]	1.38	S13
$Dy_2TiC_2@I_h(7)$-C_{80}	-1.14	-1.58	-2.29	+0.47	1.61	1100	1.13	S14
$Sc_2TiC_2@I_h(7)$-C_{80}	-0.76	-1.01	-1.96	+0.53	1.26	1400	0.89	S15

[a] $\Delta E_{EC}=E_{1/2,\,ox}-E_{1/2,\,red}$, [b] $\Delta E_{optical}=1240/onset$, [c] irreversible, [d] established from ref. S13.

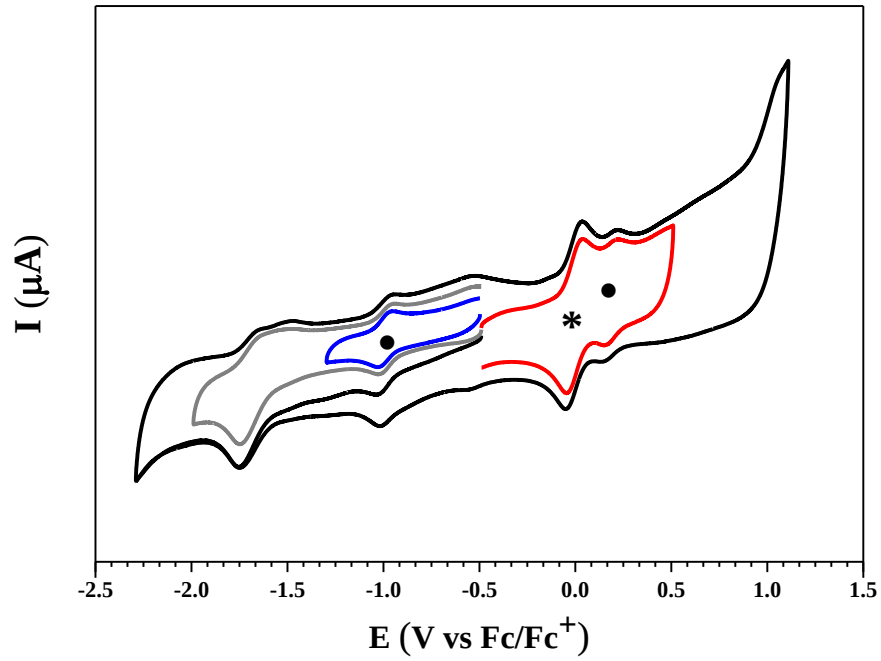

Figure S10. Cyclic voltammograms of $Dy_3C_2@I_h(7)$-C_{80} measured in *o*-DCB solution in different scanning regions showing the correlation of each reduction step with the corresponding re-oxidation step. Scan rate: 100 $mV \cdot s^{-1}$, $TBAPF_6$ as supporting electrolyte. Each redox step is marked with a number and a solid dot to aid comparison. The asterisk labels the oxidation peak of ferrocene.

References

[S1]. Dolg, M.; Stoll, H.; Savin, A.; Preuss, H., Energy-adjusted pseudopotentials for the rare earth elements. *Theor. Chim. Acta* **1989,** *75* (3), 173-194.

[S2]. Yang, J.; Dolg, M., Valence basis sets for lanthanide 4f-in-core pseudopotentials adapted for crystal orbital ab initio calculations. *Theor. Chem. Acc.* **2005,** *113* (4), 212-224.

[S3]. Weigend, F.; Ahlrichs, R., Balanced basis sets of split valence, triple zeta valence and quadruple zeta valence quality for H to Rn: Design and assessment of accuracy. *Phys. Chem. Chem. Phys.* **2005,** *7*, 3297-3305.

[S4]. Neese, F.; Wennmohs, F.; Becker, U.; Riplinger, C., The ORCA quantum chemistry program package. *J. Chem. Phys.* **2020,** *152* (22), 224108.

[S5]. Perdew, J. P.; Burke, K.; Ernzerhof, M., Generalized gradient approximation made simple. *Phys. Rev. Lett.* **1996,** *77* (18), 3865-3868.

[S6]. Laikov, D. N.; Ustynuk, Y. A., PRIRODA-04: a quantum-chemical program suite. New possibilities in the study of molecular systems with the application of parallel computing. *Russ. Chem. Bull.* **2005,** *54* (3), 820-826.

[S7]. Laikov, D. N., Fast evaluation of density functional exchange-correlation terms using the expansion of the electron density in auxiliary basis sets. *Chem. Phys. Lett.* **1997,** *281*, 151-156.

[S8]. Pipek, J.; Mezey, P. G., A fast intrinsic localization procedure applicable for ab initio and semiempirical linear combination of atomic orbital wave functions. *J. Chem. Phys.* **1989,** *90* (9), 4916-4926.

[S9]. Bader, R. F. W., *Atoms in Molecules - A Quantum Theory*. Oxford University Press: Oxford, 1990.

[S10]. Pantazis, D. A.; Neese, F., All-Electron Scalar Relativistic Basis Sets for the Lanthanides. *J. Chem. Theory Comput.* **2009,** *5* (9), 2229-2238.

[S11]. Keith, T. A. *AIMAll (Version 16.01.09), TK Gristmill Software, Overland Park KS, USA, 2016 (aim.tkgristmill.com)*, 2014.

[S12]. Tan, K.; Lu, X., Electronic structure and redox properties of the open-shell metal-carbide endofullerene $Sc_3C_2@C_{80}$: A density functional theory investigation. *J. Phys. Chem. A* **2006,** *110* (3), 1171-1176.

[S13] Fang, H.; Cong, H.; Suzuki, M.; Bao, L.; Yu, B.; Xie, Y.; Mizorogi, N.; Olmstead, M. M.; Balch, A. L.; Nagase, S.; Akasaka, T.; Lu, X. *J. Am. Chem. Soc.* **2014**, *136*, 10534-10540.

[S14] Junghans, K.; Schlesier, C.; Kostanyan, A.; Samoylova, N. A.; Deng, Q.; Rosenkranz, M.; Schiemenz, S.; Westerström, R.; Greber, T.; Büchner, B.; Popov, A. A. *Angew. Chem. Int. Ed.* **2015**, *54*, 13411-13415.

[S15] Junghans, K.; Ghiassi, K. B.; Samoylova, N. A.; Deng, Q.; Rosenkranz, M.; Olmstead, M. M.; Balch, A. L.; Popov, A. A. *Chem.-Eur. J.* **2016**, *22*, 13098-13107.